Hindawi
Journal of Nanomaterials
Volume 2019, Article ID 9082132, 10 pages
https://doi.org/10.1155/2019/9082132

Research Article

Carbon-Coated SnO_2/Ti_3C_2 Composites with Enhanced Lithium Storage Performance

Zijing Wang, Fen Wang, Kaiyu Liu, Jianfeng Zhu, and Abdul Waras

School of Material Science and Engineering, Shaanxi Key Laboratory of Green Preparation and Functionalization for Inorganic Materials, Shaanxi University of Science and Technology, Xi'an 710021, China

Correspondence should be addressed to Fen Wang; wangf@sust.edu.cn

Received 11 April 2019; Revised 14 June 2019; Accepted 31 August 2019; Published 7 October 2019

Guest Editor: Fei Ke

Tin-based anode materials including oxides, composites oxides, and tin-based alloys are identified as promising candidates for energy storage attributed to the highest theoretical specific capacity. We introduce Ti_3C_2-MXene as structural skeletons and amorphous carbon as conductive networks for tin oxide in this work. Herein, carbon-coated kernel-like SnO_2 coupling with two-dimensional (2D) layered structure Ti_3C_2-MXene ($C@SnO_2/Ti_3C_2$) composites were prepared by a hydrothermal reaction and a further calcination process. The fabricated $C@SnO_2/Ti_3C_2$ nanocomposites exhibit smaller charge transfer resistance, larger Li^+ diffusion coefficient, and better cycling stability than SnO_2/Ti_3C_2 and pure Ti_3C_2. Most of all, $C@SnO_2/Ti_3C_2$ nanocomposites display excellent initial capacity of 1531.5 mAh g^{-1} at current density of 100 mA g^{-1} and show outstanding rate performance of 540 mAh g^{-1}even after 200 cycles. In our work, we will provide a new research idea for the composite materials of metal oxides and two-dimensional layered materials in the field of electrode materials for batteries.

1. Introduction

Lithium-ion batteries (LIBs) are widely used because of their excellent specific capacity, superior cycle performance, and good safety performance. In recent years, it has become more and more widely used in mobile phones, electric vehicles, and laptops as well [1–4]. However, the current cycle stability and specific capacity of LIBs have not been able to meet the needs of the people, so it is necessary to develop LIBs with better capacity and higher cycle performance. As a new 2D transition metal carbide, MXene has a better electrochemical performance than any other carbon material in the electrode material of LIBs [5–19].

$Ti_3C_2T_x$ (T = O, OH, and F) is the most popular MXene. The 2D structure $Ti_3C_2T_x$ can be obtained by corroding the Al layer in the Ti_3AlC_2 with a ceramic structure by HF. Furthermore, Ti_3C_2-MXenes have the following excellent properties, such as lower Li^+ diffusion barrier and advanced Li storage capacity, electronic conductivity, and low operating voltage, combined with good surface hydrophilicity and excellent chemical stability and structural stability [12]. According to Sun et al.'s research, the capacity of Ti_3C_2 reaches 123.6 mAh g^{-1} at 1 C rate and a coulombic efficiency of 47% [15]. Due to these advantages and disadvantages of Ti_3C_2, it is necessary to chemically modify Ti_3C_2 with high surface area to meet the capacity requirements of the battery.

Throughout the development of lithium-ion batteries, tin-based materials are one of the most commonly used anode materials for LIBs because of their nontoxicity and excellent theoretical capacity (782 mAh g^{-1}) [20–23]. Zhu et al. used a hydrothermal method to combine SnO_2 and graphene to obtain SnO_2/G nanomaterials. SnO_2/G shows excellent electrochemical performance of 860 mAh g^{-1} after 50 cycles at 200 mA g^{-1} [24]. In Wu et al.'s work, a SnO_2/graphene nanocomposite was proposed as an anode material for LIBs by a facile method, which shows a good specific capacity of 540 mAh g^{-1} after 90 cycles [25]. According to the previous work, SnO_2-based materials have specific capacities but their capacity decays fast and the electrochemical stability needs to be improved. Therefore, it needs to be

chemically modified with B having excellent chemical stability to improve its electrochemical performance.

In our research, we have adopted a novel method to enhance the cycle stability and specific capacity of multilayer $Ti_3C_2T_x$ (T = F, OH) particles by loading SnO_2 nanoparticles (NPs) between $Ti_3C_2T_x$ layers followed by coating amorphous carbon on its surface. In previous reports, there were many methods for preparing the nanocomposite, such as Wang et al.'s preparation of the SnO_2-Ti_3C_2 nanocomposite by a hydrothermal method and using it as the anode material of the lithium-ion battery [26]. Chen and Lou used the calcination method to prepare the SnO_2 nanorods to test their electrochemical performance [27]; Zheng et al. prepared SnO_2/Ti_3C_2 nanocomposites by microwave irradiation and tested their electrochemical properties [28]. Compared with the above methods, our method has the advantages of low temperature, simple and easy operation, and low requirements on equipment; in addition, it can make SnO_2 load all the more consistently on the layers of $Ti_3C_2T_x$, improving the consistency of the SnO_2, and, in the meantime, coat the amorphous carbon all the more effectively in the calcination stage, which is an increasingly productive and advantageous approach to synthesize $C@SnO_2/Ti_3C_2$ nanocomposites. Amorphous carbon connects isolated MXene particles, and it remarkably improves the electric transportation and decreases their contact resistance by coating these voids/gaps, which makes an inordinate contribution to the electrochemical properties of the as-prepared $C@SnO_2/Ti_3C_2$ composite.

2. Materials and Methods

2.1. Synthesis Procedure. Ti_3C_2-MXene was synthesized by a solid phase calcination method as reported previously [26]. All chemicals are purchased directly and do not require further processing. $C@SnO_2/Ti_3C_2$ nanocomposites were synthesized by a hydrothermal reaction and synthesized further by the calcination process. To obtain the Ti_3C_2 solution, mix 100 mg of as-prepared Ti_3C_2 and 100 mL of ultrapure water (UPW) and then sonicate for 2 h. Then, 3.0 g polyvinyl alcohol (PVA) was added to 100 mL UPW and stirred for 30 minutes to obtain PVA solution. After this, add 12.5 g $SnCl_4{\cdot}5H_2O$ to 60 mL UPW and then add 1 mL of HCl (36.0~38.0 wt.%), mix the solution with appropriate stirring, add Ti_3C_2 solution and PVA solution to it, and then adjust the pH value to 9~10 by injecting $NH_3{\cdot}H_2O$ (25.0~38.0 wt.%). Then, the mixed solution was quickly stirred in a water bath at 85°C for 1 h and then dried at 100°C for 24 hours. Finally, under argon protection, the target product is obtained by sintering 500°C in a tube furnace and marking it as $C@SnO_2/Ti_3C_2$. As a comparative sample, SnO_2/Ti_3C_2 is prepared in the same manner as above except that there is no addition of PVA.

Figure 1 demonstrates the preparation process of $C@SnO_2/Ti_3C_2$, when solutions of polyvinyl acetate (PVA) and $SnCl_4{\cdot}5H_2O$ are thoroughly mixed. The Sn^{4+} produced by the dissolved $SnCl_4{\cdot}5H_2O$ can be combined with -OH in the uniformly distributed PVA chain, and Sn^{4+} can be uniformly distributed in the solution, so PVA is an excellent surfactant, and the $Ti_3C_2T_x$ (T = OH, F) is added. It allows the PVA chains to be oriented on the surface of the $Ti_3C_2T_x$ layers by the mutual attraction between the functional groups. After calcination process, we can obtain $C@SnO_2$-Ti_3C_2 with different structure and morphology.

2.2. Material Characterization. The characterization of the morphology and structure for the as-prepared $C@SnO_2$-Ti_3C_2 nanocomposites will be carried out in the following instruments. Morphological characterization is carried out by field-emission scanning electron microscopy (FE-SEM, S4800) and transmission electron microscopy (TEM JEM2100F) equipped with an energy dispersive X-ray analyzer (EDX). Beyond that, the composition and structure of $C@SnO_2/Ti_3C_2$ nanocomposites are characterized in X-ray diffraction (XRD, D/MAX-2500).

2.3. Electrochemical Measurements. The assemblage of lithium-ion batteries is necessary to test the electrochemical performance of as-prepared $C@SnO_2/Ti_3C_2$ nanocomposites. Right off the bat, the dynamic materials, poly(vinylidene) fluoride (PVDF), and acetylene black are completely mixed in an agate mortar at a weight proportion of 80 : 10 : 10, then N-methyl l-2-pyrrolidinone (NMP) is added dropwise, grinding is continued until the mixture was uniformly glue like, and the mixture was connected to the surface of the Cu foil by a coater, dried in a vacuum at 120°C for 12 h, and cut into small wafers. At the same time, lithium foil is used as the counter electrode, and the LIBs with the CR2032 coin type are assembled in the vacuum glove box. The electrochemical performance of the assembled battery is tested on an Ametek PARSTAT 4000 electrochemistry workstation, including cyclic voltammograms (CV) and electrochemical impedance spectroscopy (EIS). The charge and discharge performance of the gathered battery is estimated on a Land CT2001A cycler.

3. Results and Discussion

3.1. Characterization of $C@SnO_2$-Ti_3C_2. XRD patterns of as-prepared SnO_2, Ti_3C_2, and $C@SnO_2/Ti_3C_2$ nanocomposites appear in Figure 2. As shown in Figure 2(a), the Ti_3C_2, SnO_2 have a standard XRD design as detailed in the literature [5, 20]. The peaks distinguished at (002), (006), (008), and (0010) were allotted as the diffraction peaks of Ti_3C_2 [16]. The diffraction peaks of $C@SnO_2/Ti_3C_2$ nanocomposites were indexed to the (110), (101), (200), and (211) planes of tetragonal SnO_2 (JCPDS No. 41-1445). In addition, there is a small peak at about 20° demonstrating the presence of the amorphous carbon. Figure 2(b) shows partial magnification of XRD designs for these examples; the peaks at 9.28° indexed to the (002) plane move 0.43° towards 8.85°; the result shows the cross-section steady changes and the between-planar separating increments. According to the Bragg equation,

$$2d \sin\theta = n\lambda. \quad (1)$$

It can be calculated that when the (002) plane is at 9.28°, $d_1 = 9.5228$ nm is obtained; when the (002) plane is offset by

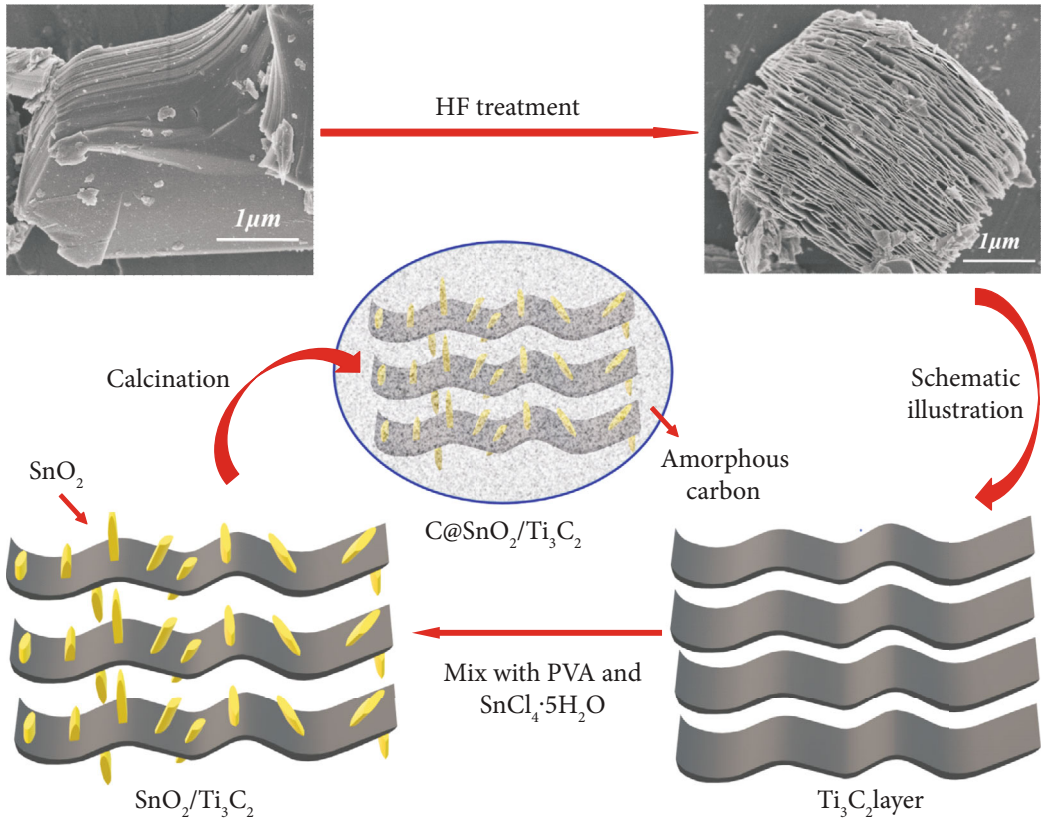

Figure 1: Synthesis schematic of $C@SnO_2/Ti_3C_2$ nanocomposites.

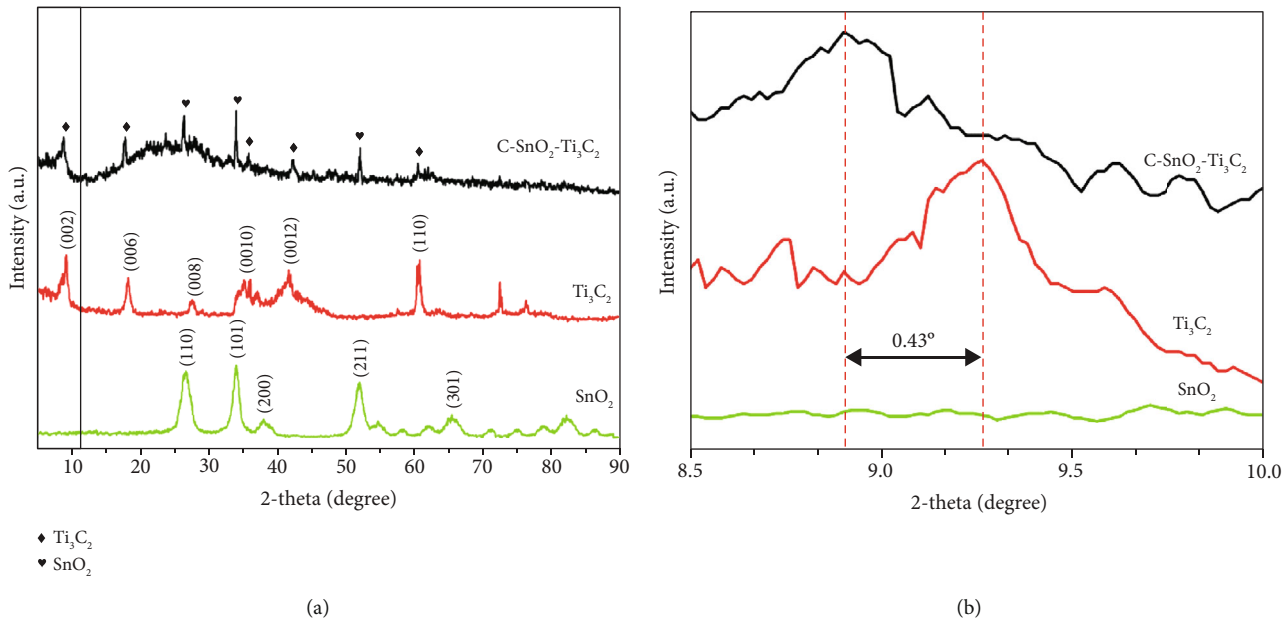

Figure 2: (a) XRD patterns of the three different samples SnO_2, Ti_3C_2, and $C@SnO_2/Ti_3C_2$; (b) partial enlargement of XRD patterns in (a).

0.43° to 8.85°, $d_2 = 9.9844$ nm is obtained, so it can be concluded that the layer spacing is increased that $\Delta d = 0.4616$ nm. This outcome demonstrates that both Ti_3C_2 and SnO_2 have been effectively prepared in $C@SnO_2/Ti_3C_2$ nanocomposites and there is no impurity.

The morphologies of the extraordinary 2D structure of Ti_3C_2, single-deck Ti_3C_2, SnO_2-Ti_3C_2, and $C@SnO_2/Ti_3C_2$ nanocomposites are seen by TEM, as shown in Figure 3. The morphologies of Ti_3C_2, single-deck Ti_3C_2, and SnO_2-Ti_3C_2 appear in Figures 3(a), 3(b), and 3(d) to compare with

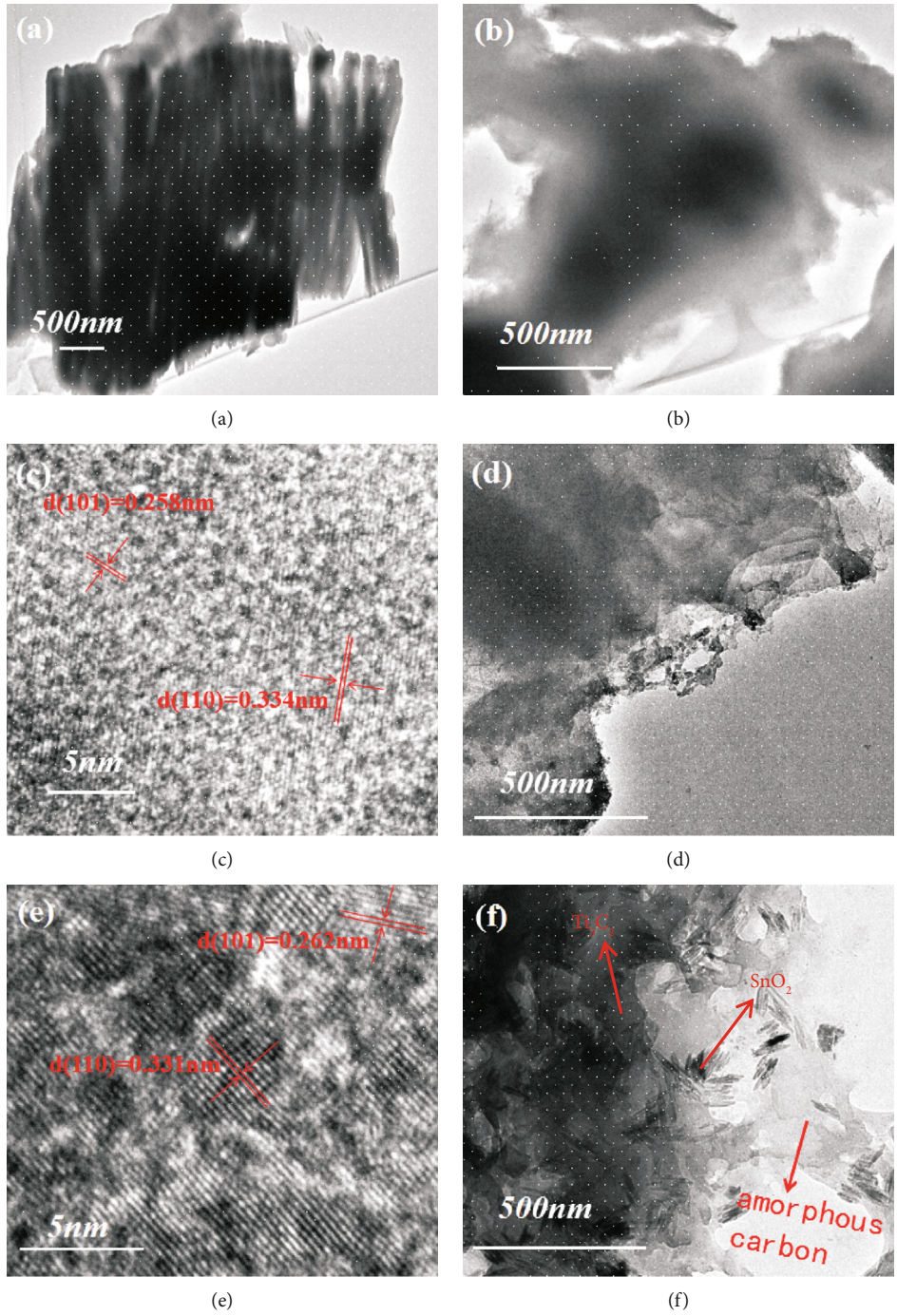

Figure 3: TEM images of $Ti_3C_2T_x$ (a) and single-deck $Ti_3C_2T_x$ nanoparticles (b); HRTEM image (c) and TEM image (d) of the SnO_2-Ti_3C_2 nanoparticles; HRTEM image (e) and TEM image (f) of the C@SnO_2/Ti_3C_2 nanoparticles.

the C@SnO_2/Ti_3C_2 composites. As can be seen from Figure 3(f), countless kernel-like SnO_2 NPs are scattered on the surface of layered $Ti_3C_2T_x$, which are about nm in size; in addition to that, it can be clearly seen that the surface of the $Ti_3C_2T_x$ sheet is covered with a large amount of amorphous carbon like a tissue. At the same time, the individual components have been marked with arrows in Figure 3(f). Corrugated amorphous carbon emerged on the surface of $Ti_3C_2T_x$ and it ensures that calcination improves the conjugated level of PVA, which can increase conductivity of C@SnO_2/Ti_3C_2 composites. Moreover, due to calcination in argon gas, the SnO_2 NPs in C@SnO_2/Ti_3C_2 with a uniform size of about 150 nm are clearly observed in Figure 3(f). From the HRTEM pictures in Figures 3(c) and 3(e), the interplanar distances of 0.331 nm and 0.262 nm may be distinguished as d (110) and d (101) of SnO_2 NPs, individually.

Figure 4 demonstrates the SEM pictures of samples. As shown in Figure 4(a), the SEM image of $Ti_3C_2T_x$ which is

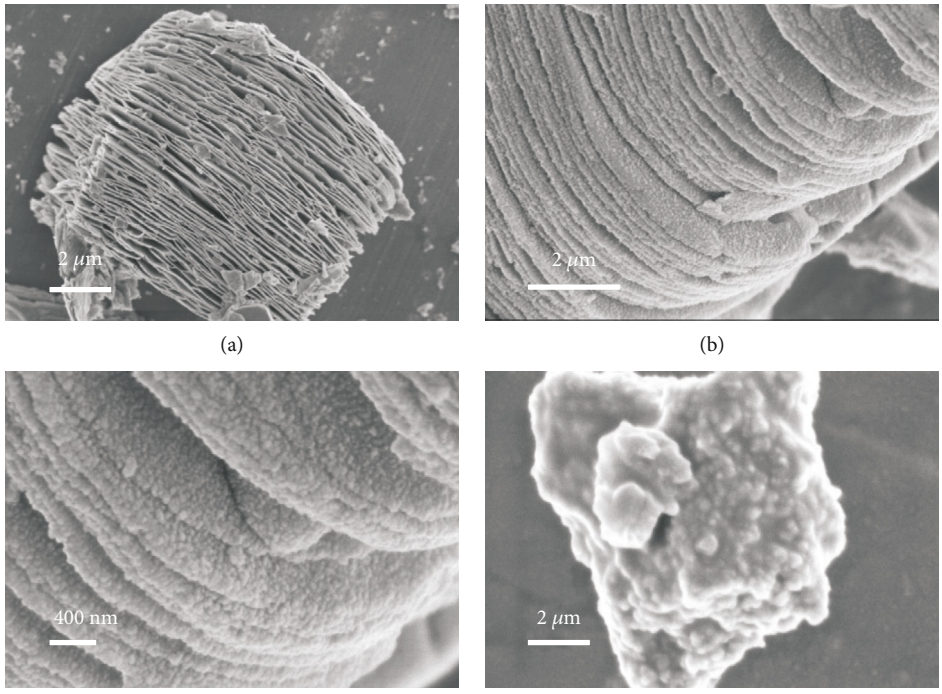

Figure 4: SEM images of $Ti_3C_2T_x$ (a), SnO_2-Ti_3C_2 nanocomposites (b, c), and C@SnO_2/Ti_3C_2 nanoparticles.

the product obtained by treating Ti_3AlC_2 with HF solution environment [5]. As can be seen from Figure 4(a), $Ti_3C_2T_x$ is an exceptionally uniform and remarkable 2D-layered structure. As observed from the SEM image of SnO_2-Ti_3C_2 (Figure 4(b)), SnO_2 nanoparticle with a particle size of around 30 nm (Figure 4(c)) is consistently upheld on the surface of $Ti_3C_2T_x$. Figure 4(d) is the SEM image of C@SnO_2/-Ti_3C_2 composites. It very well may be seen from the image that the surface of the C@SnO_2/Ti_3C_2 composite is wrapped by a layer of gauze-like amorphous carbon and the clearly visible small protrusion is SnO_2 NPs.

Elemental mapping images of C@SnO_2/Ti_3C_2 composites are shown in Figure 5. The inset in Figure 5(b) is the EDS quantitative analysis of C@SnO_2/Ti_3C_2 nanocomposites, which has the mass percentage and atomic percentage of each element. We know that the active material used in the negative electrode material of a LIB with the CR2032 coin type is about 3.76 mg, calculated from the mass percentage, and has a carbon content of about 0.7246 mg and a Ti content of about 1.9394 mg. Carbon is mainly supplied by $Ti_3C_2T_x$ and amorphous carbon. The mass of $Ti_3C_2T_x$ can be calculated according to the Ti content, and the remaining carbon is the mass of amorphous carbon. The calculated carbon content is about 0.3963 mg. The bright regions correspond to the elements tin, titanium, oxygen, and carbon. Sn, Ti, O, and C are distributed uniformly throughout the composite material, which further confirms the structure of the C@SnO_2/Ti_3C_2 composites.

3.2. Performance of C@SnO_2-Ti_3C_2 as Anodes. The electrochemical performance was assessed by utilizing the nanocomposites ($Ti_3C_2T_x$, SnO_2-Ti_3C_2, and C@SnO_2/Ti_3C_2) as working electrodes and lithium foil as the counter electrode in half-cell batteries. The thickness of the electrode and the accurate mass of active material are 300 μm and 3.76 mg, respectively. Figure 6(a) presents the CV curves of C@SnO_2/-Ti_3C_2 at a scan rate of 0.1 mV s^{-1} in the voltage range of 0.01~3.00 V (vs. Li/Li^+). As can been seen, the characteristic reduction peak was found nearly 0.69 V in the first lithiation process for the C@SnO_2/Ti_3C_2 electrode. The reduction peak of 0.69 V might be generated by the formation of a solid electrolyte interphase (SEI) layer on the surface of the active material and the formation of Li_2O while SnO_2 chemically reacts to form Sn. Nonetheless, it vanished in the following cycles, indicating that the irreversible reaction happened [9, 29]. It is important that the $Ti_3C_2T_x$ after HF corrosion has functional groups, for example, hydroxyl groups and fluorine groups. During the lithiation process, lithium ions enter the $Ti_3C_2T_x$ layer and interact with these functional groups, resulting in the irreversibility of the first cycle [15, 30]. The obvious peak near 0.02 V which compares to the lithiation of carbon rises in the active materials. In the first delithiation process, there are two distinct anodic peaks situated at 0.58 V and 1.25 V, ascribing to the dealloying process for Li_xSn and the Li ions from MXene sheets [9, 31]. The peak at 0.21 V indicates that Li ions enter the interlayer of $Ti_3C_2T_x$ to increase the capacity of lithium. C@SnO_2/Ti_3C_2 shows a couple of excellent redox peaks, suggesting C@SnO_2/Ti_3C_2 has outstanding reversible performance during charging and discharging.

EIS of $Ti_3C_2T_x$, SnO_2-Ti_3C_2, and C@SnO_2/Ti_3C_2 are shown in Figure 6(b). Nyquist plots of $Ti_3C_2T_x$, SnO_2-

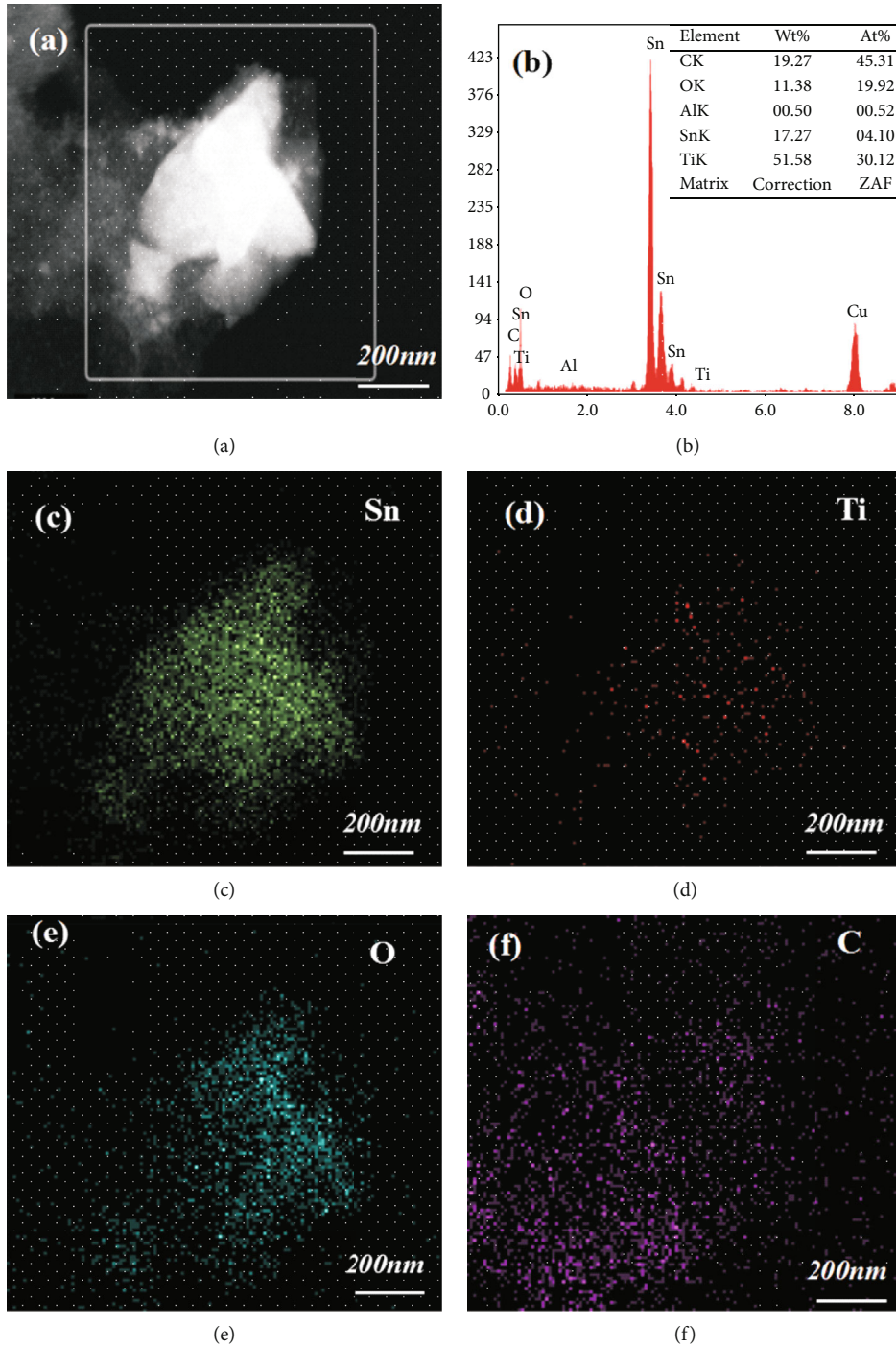

Figure 5: Elemental mapping images of C@SnO_2/Ti_3C_2 nanoparticles: (a) TEM image; (b) electron dispersive spectroscopy (EDS) pattern of (c) tin, (d) titanium, (e) oxygen, and (f) carbon distribution in the selected area.

Ti_3C_2, and C@SnO_2/Ti_3C_2 comprise a straight line at low frequencies and a semicircle at high frequencies. As can be seen from the figure, the semicircle of C@SnO_2/Ti_3C_2 is the smallest among all samples and the slope of the line of C@SnO_2/-Ti_3C_2 is the largest. Therefore, it can be concluded that the minimum impedance of C@SnO_2/Ti_3C_2 means that it has excellent conductivity, which is credited to the uniform dispersion of SnO_2 NPs and the presence of large amounts of amorphous carbon. At the same time, the increase of conductivity is beneficial to the improvement of electrochemical performance of C@SnO_2/Ti_3C_2.

With the galvanostatic charge/discharge profiles of $Ti_3C_2T_x$, SnO_2-Ti_3C_2, and C@SnO_2/Ti_3C_2 anodes at a current density of 100 mA g^{-1}, all the samples are tested over the voltage range of 0.01~3.00 V as presented in Figure 6(c). The first-cycle discharge and charge capacities of as-prepared C@SnO_2/Ti_3C_2 anodes are 811.4 and 1531.5 mAh g^{-1}, respectively, which are just about 3 times as much as that of

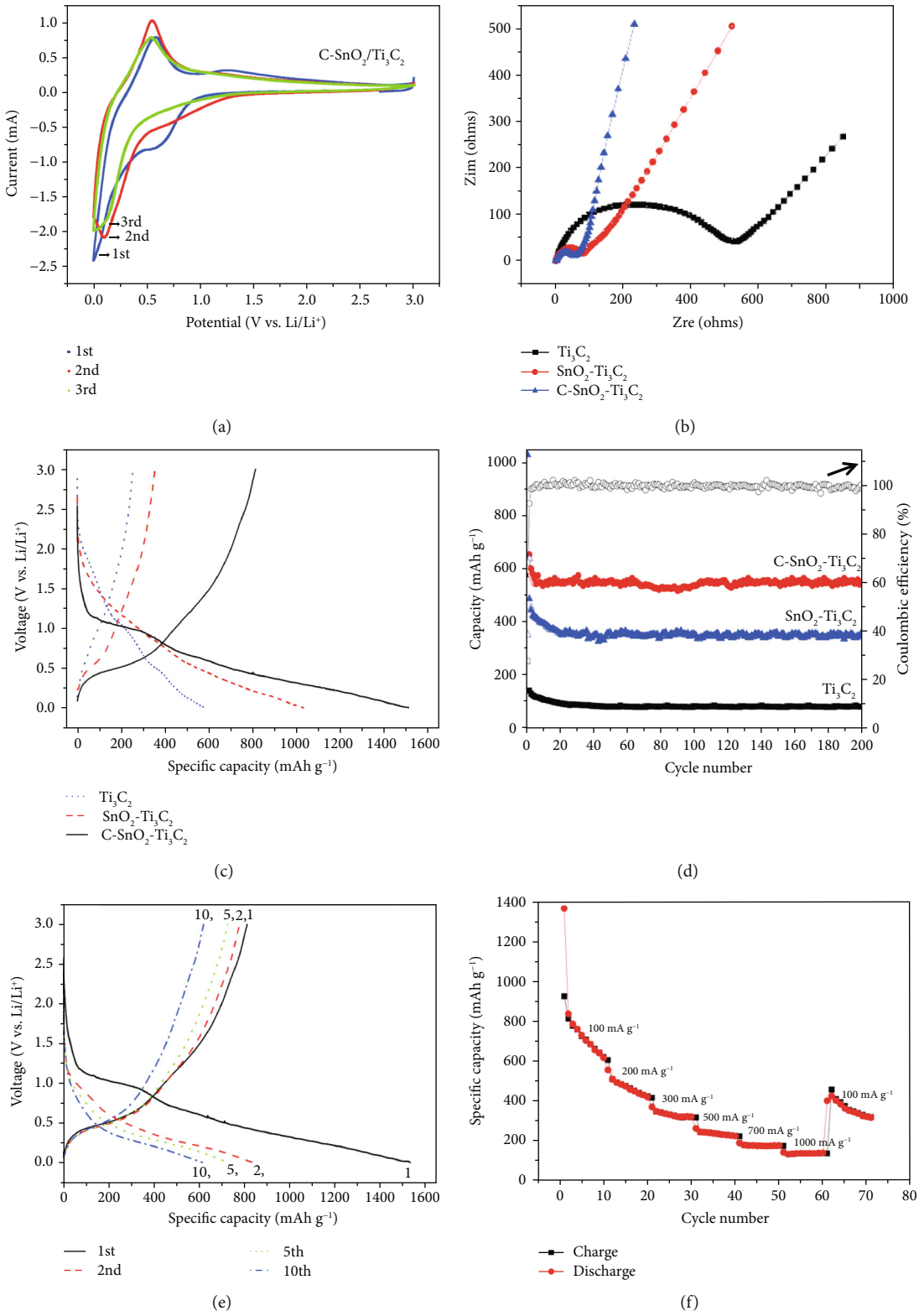

FIGURE 6: (a) CV curves of C@SnO_2/Ti_3C_2 from 3.0 V to 0.01 V vs. Li/Li^+ at a scan rate of 0.1 mV s^{-1}; (b) EIS for $Ti_3C_2T_x$, SnO_2-Ti_3C_2, and C@SnO_2/Ti_3C_2; (c) charge/discharge profiles of $Ti_3C_2T_x$, SnO_2-Ti_3C_2, and C@SnO_2/Ti_3C_2 at 100 mA g^{-1}; (d) cycling performance of $Ti_3C_2T_x$, SnO_2-Ti_3C_2, and C@SnO_2/Ti_3C_2 at 100 mA $g^{-1}$and the coulombic efficiency of C@SnO_2/Ti_3C_2; (e) charge/discharge profiles of C@SnO_2/Ti_3C_2 at 100 mA g^{-1}; (f) rate performance of the C@SnO_2/Ti_3C_2 nanocomposite electrode.

unadulterated $Ti_3C_2T_x$ (580.5 mAh g^{-1}) and higher than SnO_2-Ti_3C_2 nanocomposites (1030.1 mAh g^{-1}). The initial capacity loss is about 53% for C@SnO_2/Ti_3C_2. The voltage plateau and slope of the discharge/charge profiles correspond to the CV curves recently reported in our work. The enormous capacity decay is due to the arrangement of the SEI layer and the functional groups, including fluorine and hydroxyls, on the surface of the active material. These outcomes affirm that an exceedingly conjugated carbonaceous polymer improves conductivity and the introduction of SnO_2 NPs amplifies the d-spacing of $Ti_3C_2T_x$ layers, which expands the Li storage capacity significantly.

As shown in Figure 6(d), the first discharge capacities for the pure $Ti_3C_2T_x$ and SnO_2/Ti_3C_2 nanocomposites are 581.1 mAh g^{-1} and 1031.1 mAh g^{-1}, respectively. However, C@SnO_2/Ti_3C_2 demonstrates extraordinarily the first capacity of 1531.5 mAh g^{-1} at 100 mA g^{-1}; the first charge and discharge capacity can stay at around 540 mAh g^{-1} even after 200 cycles and the relevant coulombic efficiency of C@SnO_2/Ti_3C_2 remains at around 98% (Figure 6(d)). The outstanding electrochemical reversibility of C@SnO_2/Ti_3C_2 is attributed to the carbon coating layers. In addition to improving conductivity, the amorphous carbon can also alleviate the volume expansion of SnO_2 NPs. For a comparison, pure $Ti_3C_2T_x$ begins to decay rapidly after the third charge and discharge cycles and remains at around 82.3 mAh g^{-1} at 200 cycles. However, SnO_2-Ti_3C_2 shows lower reversible capacities than C@SnO_2/Ti_3C_2. In addition, from Figure 6(d) we can also see that the coulomb efficiency of C@SnO_2/Ti_3C_2 can still be maintained between 98% and 99% and with no significant attenuation after the tenth cycles. Moreover, C@SnO_2/Ti_3C_2 likewise has great rate capacity as appears in Figure 6(f). As the current density recovers from 1000 to 100, the capacity of C@SnO_2/Ti_3C_2 also recuperates to 454.3 mAh g^{-1}, indicating a good capacity reversibility of C@SnO_2/Ti_3C_2. It can be seen from Figure 7 that at the current density of 300 mA g^{-1}, the reversible specific capacity of C@SnO_2/Ti_3C_2 still remains at around 480 mAh g^{-1} even after 200 cycles.

Table 1 shows the electrochemical properties of different MXene-based nanomaterials as anode materials for LIBs. As can be seen from the table, the electrochemical performance of C@SnO_2/Ti_3C_2 is significantly better than other MXene-based nanomaterials. Meanwhile, the electrochemical properties of the previously reported MXene-based nanomaterials are inadmissible, especially in terms of capacity and cycle stability. In their work, storing Li^+ relies on MXene having larger lattice parameters, while larger lattice parameters imply larger layer spacing, which is beneficial for Li^+ storage [15].

However, in this paper, we rely on metal oxides (SnO_2 NPs) with high theoretical capacity to increase the Li^+ storage capacity of C@SnO_2/Ti_3C_2. At the same time, the presence of SnO_2 NPs can increase the interlayer spacing of C@SnO_2/Ti_3C_2, thereby increasing the lithium storage of the C@SnO_2/Ti_3C_2 capacity. In addition, SnO_2 NPs improve the conductivity by the transportation of Sn^{4+}, which promotes the release and insertion speed of Li^+ in the electrode material. In this way, the combination of metal oxide and MXene provides a promising research strategy for LIB anode materials.

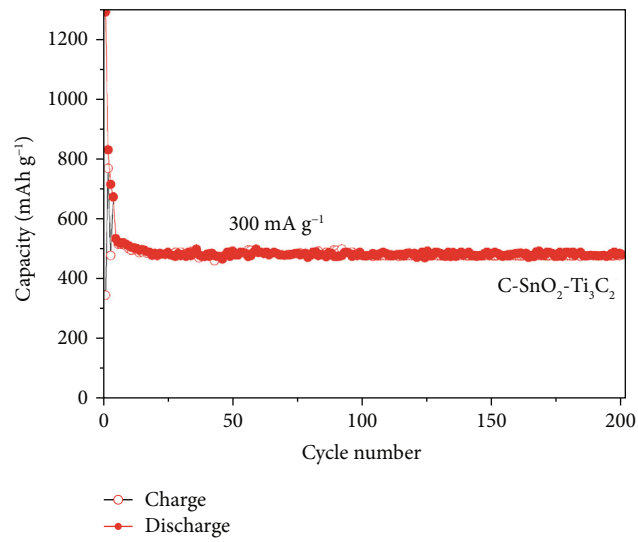

Figure 7: Cycling performance of C@SnO_2/Ti_3C_2 nanocomposite at a current density of 300 mA g^{-1}.

Table 1: Comparison of the performances of the various MXene-based materials for LIBs.

Electrode material	Current density	Initial capacity	Steady capacity/cycle number
$Ti_3C_2T_x$ [15]	260 mA g^{-1}	123.6 mAh g^{-1}	69 mAh g^{-1}/100
Ti_2CT_x [14]	260 mA g^{-1}	480 mAh g^{-1}	110 mAh g^{-1}/80
Ti_3C_2/CNF [32]	320 mA g^{-1}	848 mAh g^{-1}	320 mAh g^{-1}/80
C@SnO_2/Ti_3C_2	300 mA g^{-1}	1531.5 mAh g^{-1}	540 mAh g^{-1}/200

4. Conclusions

In this work, C@SnO_2/Ti_3C_2 nanocomposites with amazing electrochemical performance as anode material for LIBs are synthesized via hydrothermal strategy pursued by a simple calcination. Due to $Ti_3C_2T_x$ providing C@SnO_2/-Ti_3C_2 with a decent skeleton structure, amorphous carbon gives C@SnO_2/Ti_3C_2 with fantastic electrical conductivity; C@SnO_2/Ti_3C_2 nanocomposites display excellent initial capacity of 1531.5 mAh g^{-1} at current density of 100 mA g^{-1} and show outstanding rate performance of 540 mAh g^{-1} even after 200 cycles. The exceptional electrochemical performance credits the uniform dispersion of SnO_2 NPs, high conductivity of amorphous carbon, and chemical stability of $Ti_3C_2T_x$. Another reason is that SnO_2 NPs improve the conductivity by the transportation of Sn^{4+} and Li^+ insertion/extraction into the anode. These outstanding properties show that amorphous carbon and metal oxide composites in 2D-layered material MXene have comprehensive application prospects in energy storage.

Data Availability

The data used to support the findings of this study are available from the corresponding authors upon request.

Conflicts of Interest

There is no conflict of interest.

Acknowledgments

This work was supported by the National Natural Science Foundation of China (51472153, 51572158) and the Graduate Innovation Fund of Shaanxi University of Science & Technology.

References

[1] M. Armand and J.-M. Tarascon, "Building better batteries," *Nature*, vol. 451, no. 7179, pp. 652–657, 2008.

[2] Y. Li, K. Yan, H. W. Lee, Z. Lu, N. Liu, and Y. Cui, "Growth of conformal graphene cages on micrometre-sized silicon particles as stable battery anodes," *Nature Energy*, vol. 1, no. 2, article 15029, 2016.

[3] Y. H. Huang, Q. Bao, B. H. Chen, and J. G. Duh, "Nano-to-microdesign of Marimo-like carbon nanotubes supported frameworks via in-spaced polymerization for high performance silicon lithium ion battery anodes," *Small*, vol. 11, no. 19, pp. 2314–2322, 2015.

[4] C. Fang, Y. Deng, Y. Xie, J. Su, and G. Chen, "Improving the electrochemical performance of Si nanoparticle anode material by synergistic strategies of polydopamine and graphene oxide coatings," *The Journal of Physical Chemistry C*, vol. 119, no. 4, pp. 1720–1728, 2015.

[5] M. Naguib, M. Kurtoglu, V. Presser et al., "Two-dimensional nanocrystals produced by exfoliation of Ti_3AlC_2," *Advanced Materials*, vol. 23, no. 37, pp. 4248–4253, 2011.

[6] M. Naguib, O. Mashtalir, J. Carle et al., "Two-dimensional transition metal carbides," *ACS Nano*, vol. 6, no. 2, pp. 1322–1331, 2012.

[7] M. Naguib, J. Halim, J. Lu et al., "New two-dimensional niobium and vanadium carbides as promising materials for Li-ion batteries," *Journal of the American Chemical Society*, vol. 135, no. 43, pp. 15966–15969, 2013.

[8] M. Naguib, V. N. Mochalin, M. W. Barsoum, and Y. Gogotsi, "25th anniversary article: MXenes: a new family of two-dimensional materials," *Advanced Materials*, vol. 26, no. 7, pp. 992–1005, 2014.

[9] M. Naguib, J. Come, B. Dyatkin et al., "MXene: a promising transition metal carbide anode for lithium-ion batteries," *Electrochemistry Communications*, vol. 16, no. 1, pp. 61–64, 2012.

[10] O. Mashtalir, M. Naguib, V. N. Mochalin et al., "Intercalation and delamination of layered carbides and carbonitrides," *Nature Communications*, vol. 4, no. 1, article 1716, 2013.

[11] J. Hu, B. Xu, C. Ouyang, S. A. Yang, and Y. Yao, "Investigations on V_2C and V_2CX_2 (X = F, OH) monolayer as a promising anode material for Li ion batteries from first-principles calculations," *Journal of Physical Chemistry C*, vol. 118, no. 42, pp. 24274–24281, 2014.

[12] Q. Tang, Z. Zhou, and P. Shen, "Are MXenes promising anode materials for Li ion batteries? Computational studies on electronic properties and Li storage capability of Ti_3C_2 and $Ti_3C_2X_2$ (X = F, OH) monolayer," *Journal of the American Chemical Society*, vol. 134, no. 40, pp. 16909–16916, 2012.

[13] Y. Xie, M. Naguib, V. N. Mochalin et al., "Role of surface structure on Li-ion energy storage capacity of two-dimensional transition-metal carbides," *Journal of the American Chemical Society*, vol. 136, no. 17, pp. 6385–6394, 2014.

[14] S. Zhao, W. Kang, and J. Xue, "Role of strain and concentration on the Li adsorption and diffusion properties on Ti_2C layer," *Journal of Physical Chemistry C*, vol. 118, no. 27, pp. 14983–14990, 2014.

[15] D. Sun, M. Wang, Z. Li, G. Fan, L. Z. Fan, and A. Zhou, "Two-dimensional Ti_3C_2 as anode material for Li-ion batteries," *Electrochemistry Communications*, vol. 47, pp. 80–83, 2014.

[16] M. R. Lukatskaya, O. Mashtalir, C. E. Ren et al., "Cation intercalation and high volumetric capacitance of two-dimensional titanium carbide," *Science*, vol. 341, no. 6153, pp. 1502–1505, 2013.

[17] M. Ghidiu, M. R. Lukatskaya, M. Q. Zhao, Y. Gogotsi, and M. W. Barsoum, "Conductive two-dimensional titanium carbide 'clay' with high volumetric capacitance," *Nature*, vol. 516, no. 7529, pp. 78–81, 2014.

[18] Y. Dall'Agnese, M. R. Lukatskaya, K. M. Cook, P. L. Taberna, Y. Gogotsi, and P. Simon, "High capacitance of surface-modified 2D titanium carbide in acidic electrolyte," *Electrochemistry Communications*, vol. 48, pp. 118–122, 2014.

[19] M. D. Levi, M. R. Lukatskaya, S. Sigalov et al., "Solving the capacitive paradox of 2D MXene using electrochemical quartz-crystal admittance and in situ electronic conductance measurements," *Advanced Energy Materials*, vol. 5, no. 1, article 1400815, 2015.

[20] Y. Chen, B. Song, R. Chen, L. Lu, and J. Xue, "A study of the superior electrochemical performance of 3 nm SnO_2 nanoparticles supported by graphene," *Journal of Materials Chemistry A*, vol. 2, no. 16, pp. 5688–5695, 2014.

[21] Y. Idota, T. Kubota, A. Matsufuji, Y. Maekawa, and T. Miyasaka, "Tin-based amorphous oxide: a high-capacity lithium-ion-storage material," *Science*, vol. 276, no. 5317, pp. 1395–1397, 1997.

[22] M. V. Reddy, G. V. Subba Rao, and B. V. R. Chowdari, "Metal oxides and oxysalts as anode materials for Li ion batteries," *Chemical Reviews*, vol. 113, no. 7, pp. 5364–5457, 2013.

[23] J. Liang, W. Wei, D. Zhong, Q. Yang, L. Li, and L. Guo, "One-step in situ synthesis of SnO_2/graphene nanocomposites and its application as an anode material for Li-ion batteries," *ACS Applied Materials & Interfaces*, vol. 4, no. 1, pp. 454–459, 2012.

[24] Y. G. Zhu, Y. Wang, J. Xie et al., "Effects of graphene oxide function groups on SnO_2/graphene nanocomposites for lithium storage application," *Electrochimica Acta*, vol. 154, pp. 338–344, 2015.

[25] G. Wu, M. Wu, D. Wang et al., "A facile method for in-situ synthesis of SnO_2/graphene as a high performance anode material for lithium-ion batteries," *Applied Surface Science*, vol. 315, no. 1, pp. 400–406, 2014.

[26] F. Wang, Z. Wang, J. Zhu et al., "Facile synthesis SnO_2 nanoparticle-modified Ti_3C_2 MXene nanocomposites for enhanced lithium storage application," *Journal of Materials Science*, vol. 52, no. 7, pp. 3556–3565, 2017.

[27] J. S. Chen and X. W. D. Lou, "SnO_2-based nanomaterials: synthesis and application in lithium-ion batteries," *Small*, vol. 9, no. 11, pp. 1877–1893, 2013.

[28] W. Zheng, P. G. Zhang, W. B. Tian et al., "Microwave-assisted synthesis of SnO_2-Ti_3C_2 nanocomposite for enhanced supercapacitive performance," *Materials Letters*, vol. 209, pp. 122–125, 2017.

[29] X. Li, X. Wang, L. Zhang, S. Lee, and H. Dai, "Chemically derived, ultra smooth graphene nanoribbon semiconductors," *Science*, vol. 319, no. 5867, pp. 1229–1232, 2008.

[30] M. A. Hope, A. C. Forse, K. J. Griffith et al., "NMR reveals the surface functionalisation of Ti_3C_2 MXene," *Physical Chemistry Chemical Physics*, vol. 18, no. 7, pp. 5099–5102, 2016.

[31] J. Luo, W. Zhang, H. Yuan et al., "Pillared structure design of MXene with ultralarge interlayer spacing for high-performance lithium-ion capacitors," *ACS Nano*, vol. 11, no. 3, pp. 2459–2469, 2017.

[32] Z. Lin, D. Sun, Q. Huang, J. Yang, M. W. Barsoum, and X. Yan, "Carbon nanofiber bridged two-dimensional titanium carbide as a superior anode for lithium-ion batteries," *Journal of Materials Chemistry A*, vol. 3, no. 27, pp. 14096–14100, 2015.